Research Square

Preprints are preliminary reports that have not undergone peer review.
They should not be considered conclusive, used to inform clinical practice,
or referenced by the media as validated information.

Strong Field Spectroscopy of Many-Body Interactions in Solids

Daniil Kartashov

daniil.kartashov@uni-jena.de

Friedrich-Schiller University Jena https://orcid.org/0000-0002-3227-6672

Viacheslav Korolev

Institute of Optics and Quantum Electronics, Friedrich-Schiller University Jena

Thomas Lettau

Friedrich Schiller University Jena

Vipin Krishna

Institute of Solid State Physics, Friedrich-Schiller University Jena

Alexander Croy

Institute of Physical Chemistry, Friedrich Schiller University Jena

Martin Thuemmler

Institute of Physical Chemistry, Friedrich Schiller University Jena

Michael Zuerch

University of California, Berkeley https://orcid.org/0000-0001-5151-2119

Christian Spielmann

Friedrich Schiller University Jena https://orcid.org/0000-0002-5223-4170

Maria Waechtler

Institute of Physical Chemistry, Christian Albrechts University Kiel https://orcid.org/0000-0001-6073-1970

Ulf Peschel

Friedrich Schiller University Jena https://orcid.org/0000-0002-3980-9224

Stefanie Graefe

Institute of Physical Chemistry, Friedrich Schiller University Jena

Giancarlo Soavi

Friedrich Schiller University Jena https://orcid.org/0000-0003-2434-2251

Article

Keywords:

Posted Date: February 19th, 2026

DOI: https://doi.org/10.21203/rs.3.rs-8211022/v1

License: This work is licensed under a Creative Commons Attribution 4.0 International License.
Read Full License

Additional Declarations: There is **NO** Competing Interest.

Strong Field Spectroscopy of Many-Body Interactions in Solids

Viacheslav Korolev[1†], Thomas Lettau[2†], Vipin Krishna[3], Alexander Croy[4], Martin Thümmler[4], Michael Zürch[5,6], Christian Spielmann[1,7,8], Maria Wächtler[9], Ulf Peschel[2,8], Stefanie Gräfe[4,8,10], Giancarlo Soavi[3,8] and Daniil Kartashov[1,8]*

[1]*Institute of Optics and Quantum Electronics, Friedrich-Schiller University Jena, Max-Wien-Platz 1, 07743 Jena, Germany*

[2]*Institute of Condensed Matter Theory and Solid State Optics, Friedrich Schiller University Jena, Fröbelstieg 1, 07743 Jena, Germany*

[3]*Institute of Solid State Physics, Friedrich-Schiller University Jena, Helmholtzweg 3, 07743 Jena, Germany*

[4]*Institute of Physical Chemistry, Friedrich Schiller University Jena, Lessingstraße 4, 07743 Jena, Germany*

[5]*Department of Chemistry, University of California at Berkeley, Berkeley, California 94720, USA*

[6]*Materials Sciences Division, Lawrence Berkeley National Laboratory, Berkeley, California 94720, USA*

[7]*Helmholtz-Institut Jena, Helmholtzweg 4, 07743 Jena, Germany*

[8]*Abbe Center of Photonics, Albert-Einstein-Straße 6, 07745 Jena, Germany*

[9]*Institute of Physical Chemistry, Christian Albrechts University Kiel, Max-Eyth-Straße 1, 24118 Kiel, Germany*

[10]*Fraunhofer Institute for Applied Optics and Precision Engineering, Albert-Einstein-Straße 7, 07745 Jena, Germany*

Abstract

High-order harmonic generation (HHG) in solids is emerging as a versatile source of bright high-dimensional quantum light, linking the traditionally separate realms of strong-field physics and quantum optics. However, the efficiency and coherence of solid-state HHG are fundamentally limited by ultrafast dephasing of the laser-driven electron–hole polarization, an effect that rapidly destroys photon coherence and entanglement. The physical origin of this dephasing has remained elusive: introduced in theory as a phenomenological coherence time, it has largely been treated as an empirical parameter with no firm microscopic assignment. Here, we combine wavelength-dependent HHG measurements in monolayer and bulk semiconductors with *ab initio* many-body simulations revealing that momentum-resolved electron–phonon scattering is the dominant mechanism driving this ultrafast decoherence. We introduce a momentum-dependent dephasing time, obtained from first-principles electron–phonon scattering rates, which quantitatively reproduces the observed HHG yield scaling with wavelength. This concept bridges the long-lived carrier coherences of perturbative nonlinear optics and the ultrafast dephasing in strong-field HHG, providing a unified description of many-body dynamics in both regimes. Our findings resolve the long-standing debate concerning ultrafast many-body decoherence and open the door to mitigating decoherence in strongly driven solids – paving the way for practical quantum-optics applications of HHG, such as compact sources of entangled photons for quantum technologies.

High-order harmonic generation (HHG) in solids occurs when an intense laser field drives electrons from the valence to the conduction band and accelerates them across the Brillouin zone within a single optical cycle, inducing ultrafast oscillating intraband currents and interband polarization[1-5]. This nonperturbative frequency-conversion process can generate a broad coherent spectrum from the infrared to the extreme-ultraviolet (XUV), enabling tabletop attosecond pulse sources and new modalities of ultrafast spectroscopy[6-16]. In contrast to atomic gases, where a single active electron picture often suffices, HHG in solids is inherently a multiparticle phenomenon: the strong-field excitation creates electron–hole pairs whose coherent polarization radiates high-order harmonics[1-5]. As a result, solid HHG is exquisitely sensitive to many-body interactions that dephase the electron–hole motion. Indeed, the interband recombination mechanism – the solid-state analogue of the atomic three-step model – relies on phase-locked electron and hole trajectories, which are easily disrupted by scattering processes. Such decoherence has no counterpart in gas HHG and must be accounted for in solids: in theory, this is done by introducing a polarization decoherence time on the order of only a few femtoseconds[1-3]. Strikingly, the physical origin of this ultrafast dephasing has remained unclear, and the required dephasing times are far shorter than those known from conventional weak-field nonlinear optics[17,18]. For example, excitonic resonances and low-order nonlinearities in semiconductors typically exhibit coherence times of hundreds of femtoseconds to picoseconds[17,18], whereas replicating solid HHG spectra has demanded dephasing times on the order of 2–10 fs[1-3]. This discrepancy fueled debate, with some studies suggesting that an ultrashort dephasing time might not be intrinsic but rather an artifact avoidable by considering propagation effects[19]. Overall, a deeper understanding of the microscopic origin and timescale of dephasing in solid HHG has been one of the most important open questions in the field[20,21], as it directly impacts our ability to model, predict, and harness HHG in novel materials.

Beyond its classical aspects, solid HHG has recently attracted attention as a source of quantum light. Experiments in atomic HHG first revealed quantum-optical signatures in high harmonics, sparking the idea that strong-field processes can generate entangled photons despite involving macroscopic photon fluxes[22-30]. Very recently, HHG in semiconductors has been shown to produce nonclassical light: violating multi-mode Cauchy–Schwarz inequalities and exhibiting two-mode squeezing in the emitted harmonics[31]. These observations position solid-state HHG as a promising route to generate bright entangled photon states, bridging ultrafast nonlinear optics with quantum information science. Crucially, however, any quantum coherence or entanglement in the HHG output will be limited by the electron–hole dephasing during the nonlinear interaction. Ultrafast dephasing (i.e. femtosecond-scale polarization decay) in the solid effectively acts as an ultrafast decoherence mechanism, wiping out phase information and entanglement between photons if it occurs before harmonic radiation is emitted. Identifying and overcoming the sources of this dephasing is thus critical for pushing solid HHG into the quantum regime.

In this work, we tackle the dephasing problem head-on through a combined experimental and theoretical approach. We perform wavelength-dependent HHG

measurements on monolayer WS_2, MoS_2 and a bulk CdSe film to sensitively probe the influence of dephasing on the emitted harmonic yield. In our experiments, the total high-harmonic output drops precipitously as the drive wavelength increases, with a steeper efficiency fall-off than in atomic gases[32]. We find that the power-law scaling of HHG yield with wavelength in each material (exponents ranging from approximately –6 to –9) cannot be explained by conventional models assuming a fixed, long coherence time – instead, it points to an intrinsic dephasing on ultrafast timescales. To interpret these results, we carry out *ab initio* real-time simulations and many-body calculations of electron scattering rates. By systematically considering various scattering mechanisms, we identify electron–phonon scattering as the dominant source of dephasing in solid HHG. Notably, in the strong-field regime, electrons are driven to high crystal momenta across the Brillouin zone, where the electron–phonon coupling is highly momentum-dependent. Our calculations predict that while near the band-edge (e.g. at the K-valley of WS_2) electron–phonon scattering is relatively slow (with scattering times on the order of ~200 fs at room temperature), electrons driven to larger momenta experience much faster dephasing – on the order of just a few femtoseconds – due to increased electron–phonon interaction strength. This pronounced dispersion in scattering rates with crystal momentum provides a natural explanation for the so far empirically short dephasing times in HHG. We therefore introduce a momentum-dependent dephasing time T_2, defined according to *ab initio* electron–phonon scattering lifetimes, as a physically grounded replacement for the ad hoc constant dephasing time used in prior models[1-3,33]. Incorporating a k-dependent dephasing time into our simulations yields excellent agreement with the observed HHG wavelength scaling and spectra across all tested materials. This momentum-resolved dephasing model unifies the description of ultrafast many-body dynamics in both the perturbative (weak-field) and nonperturbative (strong-field) regimes of solid-state optics, as it converges to long T_2 values in the low-excitation limit and to ultrashort T_2 in extreme driving fields. In summary, by pinpointing electron–phonon scattering as the principal cause of HHG dephasing and by formulating a robust k-dependent dephasing framework, we provide a comprehensive solution to the dephasing puzzle in solid HHG and set the stage for strategies to control decoherence in future strong-field materials.

Results

High harmonic spectra of atomically thin and bulk semiconductors. The experiments are carried out on monolayer WS_2 and MoS_2 transition metal dichalcogenides (TMDs) to avoid the influence of linear and nonlinear propagation effects. Further, we compare the results of atomically thin semiconductors to HHG obtained from a bulk polycrystalline CdSe thin film. TMD monolayers were obtained by mechanical exfoliation and transferred onto a c-cut sapphire substrate (see Supplementary Section 1). The bulk, polycrystalline, 140 nm thick, wurtzite symmetry CdSe film was prepared directly on the sapphire substrate *via* chemical bath deposition. We excite the samples with intense (up to 1.5 TW/cm^2) femtosecond mid-IR pulses at different wavelengths in the range λ= 3-5 μm and measure high-order harmonic spectra within the

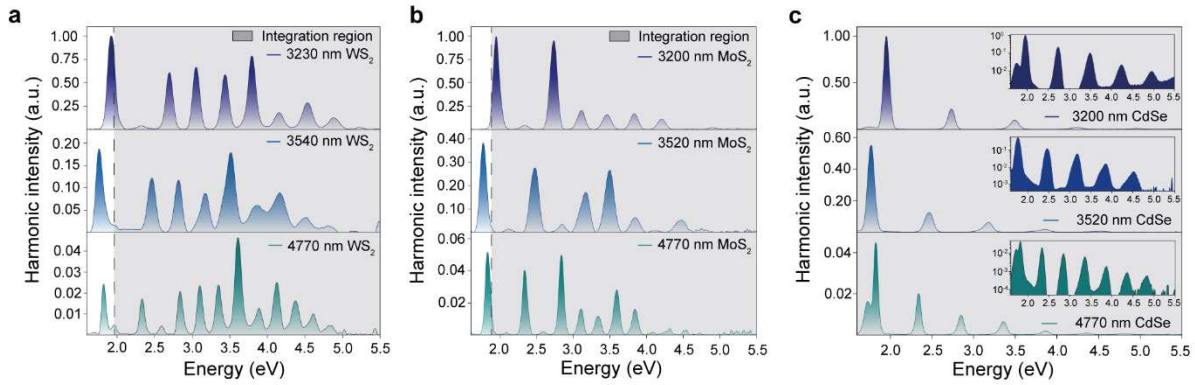


Fig. 1 Wavelength dependence in solid-state HHG. HHG spectra on linear scale, corrected to the spectrometer and the detector sensitivity, for three selected laser wavelengths from (**a)** WS_2 along the zigzag direction, (**b)** MoS_2 along the zigzag direction and (**c)** CdSe polycrystalline film. The inset figures are the same, but in logarithmic scale for better visibility. The shaded area on all figures marks harmonics with energies of quanta above the bandgap (dashed line) and represents the integration region for the harmonic yield. Note the different y-axis range for the different driving wavelength, indicating the reduced harmonic yield for longer driving wavelengths.

0.2-1 μm spectral region at a constant laser intensity (see Methods and Supplementary Section 2). In our analysis, we focus on harmonics with photon energies larger than the electronic bandgap, i.e., those that are generated predominantly by the interband mechanism.

Fig.1 shows selected high harmonic spectra obtained from two different TMD monolayers (a, b), oriented along the zigzag direction relative to the laser polarisation, and from the CdSe film (c) at a peak intensity of approximately 1.5 TW/cm^2. In TMD monolayers, for symmetry reasons, both even and odd harmonics are generated up to 5 eV, and the spectra exhibit a clear plateau behaviour with a cut-off near 4 eV. In contrast, harmonic spectra measured from the bulk CdSe contain only odd orders, and the intensities exponentially decay with increasing harmonic order. This can be explained by strong re-absorption of photons with energies above the bandgap (1.64 eV) of the material[34]. Note that for a thickness of 140 nm, CdSe film dispersion effects like phase and group velocity mismatch are negligible in the entire spectral range of harmonic measurements.

Experimental wavelength dependence. Fig. 2 displays the experimentally retrieved wavelength dependence of the integral harmonic yield, measured at different pump laser wavelengths but at a fixed laser intensity of 1.45 TW/cm^2 (for details on the intensity calibration, see Supplementary Section 1). The presentation on a double logarithmic scale allows convenient fitting of a power-law decay λ^{-x} with a linear function, characterising the power index x of its decay by the value of the slope. For monolayer WS_2 (Fig. 2a), we find values of the power index of -8.9 ± 1 and -8.2 ± 0.9 along the zigzag and armchair directions, respectively. Similarly, Fig. 2b shows the wavelength dependence of the total HHG yield from a MoS_2 monolayer along the zigzag and

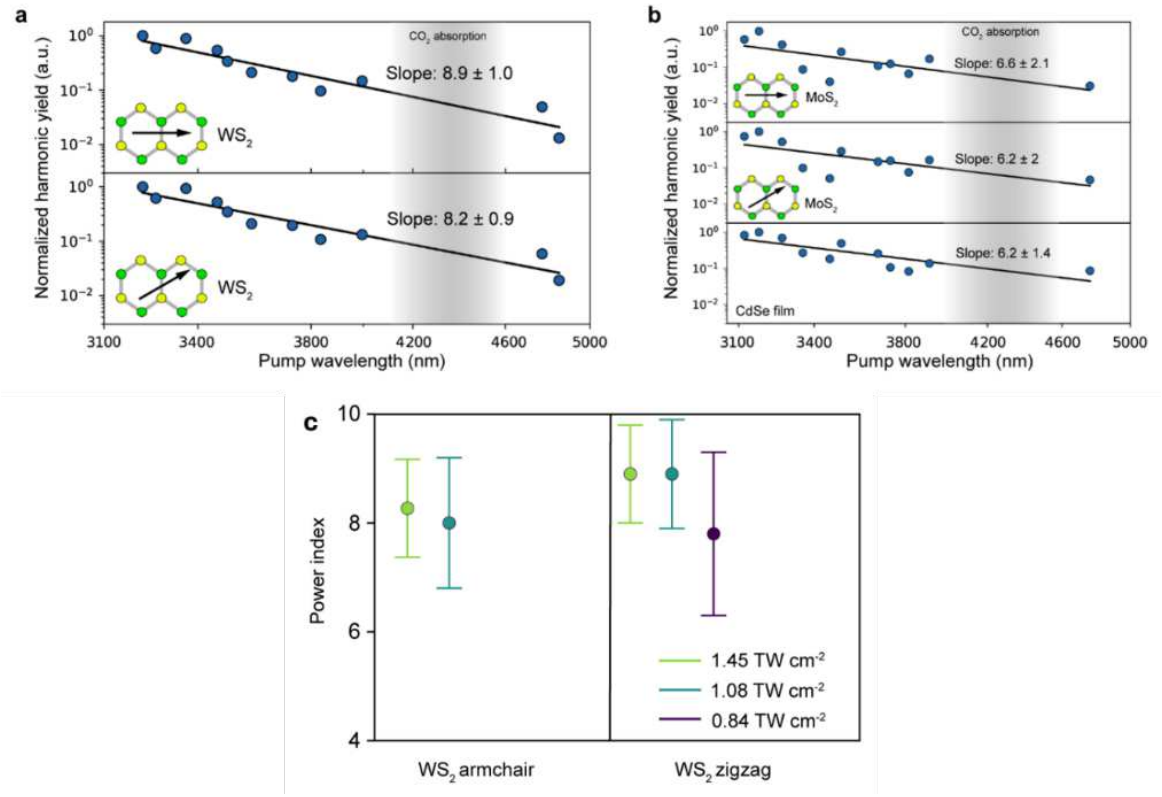


Fig. 2 Wavelength dependence of the high harmonic yield. **a** Normalised harmonic yield (blue dots) as a function of the pump wavelength plotted in a double logarithmic scale from a monolayer WS_2 along the zigzag (top figure) and the armchair (bottom figure) directions. **b** The same for MoS_2, top figure along the zigzag direction, middle along the armchair and bottom for CdSe film. The values represent the integrated harmonic yield in the spectral region above the bandgap (marked in Fig.1). The black line shows a linear fit and the absolute values of the slopes are shown. The shaded grey area represents the CO_2 absorption region, where measurements are not possible under ambient conditions. The laser intensity was fixed to 1.45 TW/cm^2. **c** Experimentally measured dependence of the power index in the wavelength-dependent decay of the harmonic yield on the driving laser intensity, for two different crystal orientations of WS_2.

armchair directions and from the CdSe film, with retrieved indices -6.6 $\pm$ 2 (MoS_2 zigzag) and -6.2 $\pm$ 1.4 (both MoS_2 (armchair) and CdSe). The power indices are only weakly dependent on the laser intensity, remaining almost unaffected (< 10%) when latter is changed by more than 70% (Fig. 2c). Note that in all cases, the harmonic yield does not decay monotonically but shows an oscillatory behaviour instead. Similar oscillations have been numerically found before and were assigned to quantum path interferences[33]. In general, the experimentally retrieved power index is significantly larger than the theoretically proposed λ^{-4} dependence expected assuming an infinite dephasing time (no dephasing processes)[33].

Scattering processes and k-dependent dephasing time. To elucidate the origin and impact of the dephasing time in HHG of solids, we performed extensive numerical and theoretical studies: We conducted ab-initio real-time time-dependent density functional (rt-TDDFT) calculations of HHG in a WS_2 monolayer, showing $\lambda^{-3.3}$ dependence and strong oscillations (Supplementary Section 3, Fig. S4a). Further, we numerically solved

the two-dimensional semiconductor Bloch equations (SBE) without a dephasing time (see Methods and Supplementary Section 5 for details). The results of SBE simulations are in excellent agreement with the results of rt-TDDFT calculations yielding a $\lambda^{-3.4}$ dependence and strong oscillations (Supplementary Section 3, Fig.S4b). Thus, both models that do not include the dephasing time explicitly fail to describe the much steeper experimentally measured dependence of the harmonic yield on the driving wavelength.

To identify the physical origin of ultrafast dephasing, we recapitulate possible scattering processes occurring in solids: (i) The first collisional process, carrier multiplication, is much more efficient in 2D materials than in bulk semiconductors due to quantum confinement[35,36,37]. However, this process becomes efficient only if the excited electron has an excess energy equal or larger than the bandgap (*i.e.*, a total energy larger than twice the bandgap), which is possible by single or several photon absorption from a light source with large photon energy. Under the conditions of strong-field excitation with photon energies much smaller than the bandgap, as it is realised in our experiments, the electron tunnels to the bottom of the conduction band, making carrier multiplication in TMDs inefficient and, thus, negligible. This was confirmed in experiments on transport phenomena under DC voltage where the carrier multiplication was identified primarily due to the carrier contribution from trap defects states[38,39].

The second scattering process that can contribute to the dephasing in HHG is electron-electron scattering (ii)). Electron-electron scattering depends sensitively on the number of excited carriers. Thus, higher intensity leading to a substantial increase of excited carriers should strongly impact the power index if electron-electron scattering was the major contribution to dephasing. Recent experiments on influence of photo-doping on HHG in 2D materials have shown that, under conditions of high density of the excited carriers, when screening effects can be neglected and electron-electron collisions play the major role, the dephasing time scales with the electron density as $\sim 1/N_e$[40]. Based on the Keldysh strong-field excitation rate in semiconductors[41,42], we estimate that the carrier density increases by approximately up to one order of magnitude for the laser intensity variation investigated in our work. According to our numerical simulations and results from Ref.33, such variation in the dephasing time would be reflected in a significant change of the power index, which however, is not observed in our experiments (Fig.2c). Thus, we conclude that electron-electron scattering plays a minor role in the dephasing responsible for the steep slope in the dependence of the harmonic yield on the driving wavelength.

Finally, we consider the contribution of electron-phonon scattering (e-ph scattering, iii). Using DFT methods, we calculate the total (summed over all phonon modes) band-specific electron-phonon scattering time in WS_2 (see Supplementary Section 4 for details), see Fig. 3. The striking feature of the scattering time is its pronounced dependence on the electron lattice momentum. In the first conduction band, it drops abruptly from ≈200 fs at the K-points to below 10 fs as soon as the electron leaves the K-valley and reduces to ≈2 fs in the vicinity of the Γ-point (Fig. 3a). A similar ultrashort time scale is found in the valence band for the hole-phonon scattering (Fig. 3b). From the band-specific scattering times, we introduce the k-dependent polarisation dephasing time

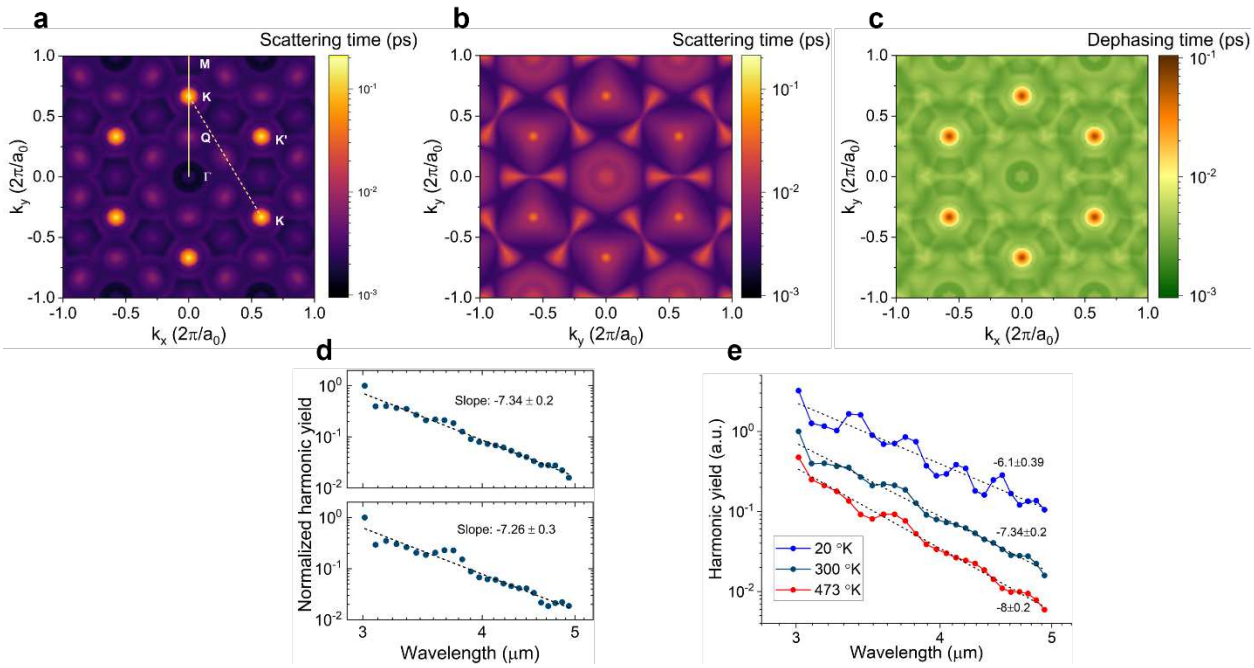


Fig. 3 Numerical simulations for the k-dependent electron-phonon scattering time. Two-dimensional map of **a** electron-phonon scattering time in the first conduction band and **b** hole-phonon scattering time in the valence band. Note the logarithmic scale for the false colour, showing the scattering time. The solid line depicts electron motion in the band along zigzag direction, the dotted line – along the armchair direction. Also, high symmetry points are marked. **c** Corresponding polarisation dephasing time between the valence and the first conduction bands, see text. **d** Normalised harmonic yield as a function of the pump wavelength for the zigzag (top figure) and the armchair orientations (bottom figure), calculated by SBE with $T_2 = T_2(k)$ shown in panel c. **e** Wavelength dependence of the harmonic yield for different lattice temperatures. The dotted lines are the linear fits with the slopes marked in the figure.

$T_{2,mn}(k)$ between two bands m and n as $\frac{1}{T_{2,mn}(k)} = \frac{1}{2}\left(\frac{1}{\tau_m(k)} + \frac{1}{\tau_n(k)}\right)$ (see Supplementary Section 5 for details). The corresponding dephasing time map between the valence and the first conduction bands is shown in Fig.3c. This dephasing time enters the two-dimensional SBE (see Methods and Supplementary Section 5 for details) to simulate HHG. Fig. 3d displays such calculated wavelength dependence of the harmonic yield for the laser pulse parameters and the spectral integration range used in the experiments. The retrieved slope of 7.3±0.2 (7.2±0.4) for the zigzag (armchair) orientation agrees rather well with the values retrieved from the experimental measurements. The non-perfect match between the experimental and simulated power indices might be due to the following reasons. First, as shown in Ref. 33 and confirmed by our simulations (see Supplementary Section 6), the value of the power index is exponentially sensitive to the precise value of the dephasing time. Second, and more important, we calculated the electron-phonon scattering rates within a field-free perturbation theory approach (see Supplementary Section 4). Clearly, these rates might be noticeably different in the strong field regime, when the bands are dynamically modified and the electron energy distribution is far from equilibrium. However, such new theory of ultrafast strong field e-

ph scattering needs to be developed, and the approach used in our work is currently the only feasible one.

The numerical simulations also reproduce the oscillations in the dependence of the harmonic yield on the driving wavelength (Fig.3d). These oscillations were attributed before to quantum path interference for HHG in gases[43] and solids[33]. Detailed investigation of these oscillations is subject of separate work. Here, we would like to note that the amplitude of the oscillations is directly linked to the value of the dephasing time: Larger values of the dephasing time result in increased amplitudes of the oscillations. Therefore, the modulation amplitude might be used as well as an indicator of the dephasing process' timescales.

The identified origin of the dephasing as e-ph scattering suggests that the dephasing time might be temperature dependent. Indeed, further, numerical simulations performed for a lattice temperature of 20 ˚K predict that the scattering time increases in the K (K') valley up to 1 ps and by a factor 2-3 across the band, remaining ≈3 fs near the Γ- point (see Supplementary Fig. S6). The calculated scattering time at low temperatures suggests that the processes of phonon emission in electron-lattice collisions play the dominant role. Also, the increased values at low temperatures predict significant increase in the harmonic yield. This is indeed confirmed by the numerical simulations, showing a reduction in the power index and up to one order of magnitude increase of the harmonic yield at long wavelengths (Fig.3e). Noteworthy, also the amplitude of the oscillations increases significantly, mirroring longer dephasing time. Thus, our simulations suggest a possibility for a direct experimental determination of the contributions of the electron-electron and electron-phonon scatterings by conducting wavelength- and temperature-dependent HHG measurements for different laser intensities.

Simulations for monolayer MoS_2 provide very similar results with slightly larger scattering times, that may explain the difference in the slopes retrieved for MoS_2 and WS_2 monolayers. Also, for CdSe in wurtzite structure, as for the TMD monolayer, the scattering time is strongly k-dependent and drops abruptly from ≈100 fs at the Γ-point to a few femtoseconds for larger lattice momenta (see Supplementary Fig.7). Therefore, the ultrashort nature of the e-ph scattering outside the bandgap minima is a universal phenomenon in solids, now experimentally assessable by the nonlocal processes of HHG.

Discussion

In conclusion, we have identified the microscopic origin of the ultrafast dephasing that has long been recognized as a key limiter in solid-state HHG. Through joint experiments and *ab initio* simulations, we measured how the high-harmonic yield in two-dimensional and bulk semiconductors sharply decays with increasing laser wavelength, revealing material-specific scaling exponents (approximately λ^{-6} to λ^{-9}) steeper than those in atomic gases[32]. This precipitous drop in efficiency directly reflects the presence of a very short dephasing time in the solid HHG process. By analyzing all relevant scattering pathways, we pinpoint electron–phonon collisions as the dominant dephasing mechanism in the interband HHG process. Our calculations show that an electron driven by a strong

field experience highly momentum-dependent decoherence: near the band extrema, dephasing is relatively slow (hundreds of femtoseconds), but at higher crystal momenta it accelerates to just a few femtoseconds due to the sharply increasing electron–phonon scattering rates. This finding explains why solid HHG effectively operates with an ultrashort coherence time – the laser field sweeps electrons into regions of k-space where phonon-induced decoherence is almost instantaneous.

By introducing a k-dependent dephasing time informed by first-principle scattering calculations, we bridge the gap between earlier conflicting pictures of dephasing in solids. Specifically, our model reconciles the disparate timescales used in previous weak-field and strong-field descriptions: what had been treated as an empirical T_2 constant tied to the optical cycle is now understood as an average over momentum-dependent scattering rates, which naturally varies with driving field and material. This insight finally resolves the long-standing debate regarding the role and origin of dephasing in solid HHG. Moreover, the momentum-resolved dephasing concept unifies the interpretation of ultrafast nonlinear optical phenomena across regimes, showing that the extreme excitation of carriers to high energies is the key factor that differentiates strong-field HHG from conventional perturbative processes. In different materials and under different laser conditions, the effective coherence time will depend on how far into the Brillouin zone the electrons are driven – providing a clear explanation for the wide range of dephasing times reported in past experiments and simulations. Our work thus establishes a firm microscopic foundation for the dephasing time in solids, replacing ambiguity with quantitative predictability.

Looking forward, these results have significant implications for both fundamental and applied photonics. First, knowing that electron–phonon scattering sets the fundamental limit to coherence in solid HHG enables new strategies to mitigate decoherence. For instance, material engineering or environmental control (such as cryogenic operation to reduce phonon activity) could extend the effective T_2 and boost harmonic efficiency. Such control over ultrafast dephasing would directly benefit the development of compact attosecond pulse sources and frequency combs in solids, whose performance is currently constrained by limited harmonic yield. Second, and crucially, suppressing electron–phonon dephasing opens a pathway to preserve quantum coherence in the HHG process. This could allow the generation of nonclassical light at high photon energy and fluxes, effectively turning solid-state HHG into a bright source of entangled photons and squeezed light. By leveraging materials with weaker electron–phonon coupling or dynamically altering phonon interactions (e.g. via phononic excitation or strain), one could envision solid-state high-harmonic devices that produce large numbers of entangled photons on ultrafast timescales – a powerful resource for quantum optics and communication. In summary, by uncovering and controlling the electron–phonon decoherence in strong field-driven solids, our work paves the way toward scalable quantum photonic technologies based on high-harmonic generation. The convergence of strong-field physics with quantum optics promises not only deeper insight into light–matter interaction at extreme conditions, but also practical advances in ultrafast quantum light sources built on solid-state platforms.

Methods

Experiments

A Ti:sapphire-based regenerative amplifier (Coherent Astrella, 800 nm central wavelength, 35 fs pulse duration at 1 kHz repetition rate) was used to pump an optical parametric amplifier (Light Conversion TOPAS), followed by a noncolinear difference frequency generation (NDFG) module, offering ultrashort pulses with the duration from 60 to 100 fs in a spectral region from 3 to 12 μm. To ensure that the wavelength-dependent measurements were conducted under fixed peak intensity conditions, the pulses were characterised temporally, using the second harmonic frequency-resolved optical gating (SH-FROG) method, and spatially, using a mid-IR CCD camera for measuring a focal intensity distribution. The dependence on the pump energy was measured for all wavelengths. The harmonics were measured in the 200 - 1100 nm wavelength range, limited by the spectrometer and the detector. All spectra were normalised on the camera and the grating sensitivity and recalculated in the frequency domain before yield integration. The resulting yield for each laser wavelength was interpolated as a function of the laser peak intensity. The final data were acquired from interpolation (see Supplementary Note 2). The experimental setup is shown in Supplementary figure S1. A laser beam was attenuated by a pair of wire-grid polarisers on a silicon substrate and focused by a 50 mm CaF_2 lens at a normal incidence onto a TMD/CdSe sample deposited on a c-cut sapphire substrate. Pump polarisation was tuned by a broadband half-wave plate (B-Halle). Harmonic emission is collected by a CaF_2 f=25 mm lens in transmission geometry and measured by a Kymera-328i spectrometer equipped with a cooled UV-enhanced CCD camera. An on-site microscopy setup with an x50 objective lens (NUV Plan Apo 0.45 NA) was implemented for optical diagnostics and alignment of the samples. All experiments were performed at ambient conditions.

Numerical simulations

The geometry and the electronic structure of single-layer WS_2 were calculated using density functional theory as implemented in Quantum Espresso[44]. Phonon properties were obtained within density functional perturbation theory using the same software. For all calculations, we used the SG15 optimised norm-conserving pseudo-potentials[45,46] from http://www.quantum-simulation.org/potentials/sg15_oncv/index.htm. A kinetic energy cutoff for the wavefunction of 90 Ry was applied, and the PBE functional was used in all cases[47]. To ensure a sufficient decoupling of adjacent layers, we added about 19.4 Å of vacuum in the direction perpendicular to the layer. For the electron and phonon calculations, we used Monkhorst-Pack meshes with 18x18x1 and 9x9x1 points, respectively. The electronic band-structure and the phonon dispersions are shown in Supplementary Figure 5. The electron-phonon induced finite lifetime of the electronic states was obtained using the electron-phonon Wannier functions (EPW) approach[38,49]. It is calculated from the imaginary part of the electron-phonon self-energy for the respective Bloch state as in Ref. 50. For the integration over the Brillouin zone, we used 27x27x1 *k*-points and a very fine mesh of 500x500x1 *q*-points to assure convergence.

The rt-TDDFT calculations were carried out using the Octopus code[51] with the “hgh_lda” pseudopotentials, the semicore set of Hartwigsen-Goedecker-Hutter in the local density approximation[52]. The simulations converged for a Brillouin zone sampling of 40×40 and a real-space mesh with 0.3 Bohr spacing.

For the SBE simulations, we followed the approach outlined in Ref. 2. To calculate the energy bands and transition dipole elements as well as Berry connections, we used a three-band tight-binding model[53] including one valence and two conduction bands and spin-orbit coupling. The details of SBE model are elaborated in the Supplementary Section 5.

Acknowledgments

The authors highly acknowledge funding by the German Research Foundation DFG (CRC 1375 NOA – Nonlinear Optics down to Atomic scales), project number 398816777 (projects C4, A1). M.Z. and C.S. acknowledge funding by the Federal Ministry of Education and Research (BMBF) under the "Make our Planet Great Again – German Research Initiative" (grant 57427209) implemented by the German Academic Exchange Service (DAAD)

Authors contribution

V.Ko. build the experimental setup, carried out experimental measurements and data processing, T.L. and M.T. conducted rt-TDDFT and SBE numerical simulations, V.Kr. prepared and characterised the monolayers, A.C. conducted DFT calculations for band structure and electron-phonon scattering rates, M. Z. contributed by the laser system, results discussion, and interpretation, C.S. supervised the experimental research, M.W. synthesised the CdSe film, U.P. and S.G. supervised the numerical simulations, contributed to results analysis and interpretation, G.S. supervised monolayer manufacturing, contributed to results analysis and interpretation, D.K. conceived the idea, supervised the experimental measurements, contributed to data processing and interpretation. V.Ko., S.G. and D.K. wrote the manuscript with contribution from all co-authors.

† These authors contributed equally

References

1. Vampa, G., Brabec, T. Merge of high harmonic generation from gases and solids and its implications for attosecond science. *J. Phys. B* **50**, 083001 (2017).
2. Vampa, G., McDonald, C. R., Orlando, G., Klug, D. D., Corkum, P. B., Brabec, T. Theoretical Analysis of High-Harmonic Generation in Solids. *Phys. Rev. Lett*. **113**, 073901 (2014).
3. Yue, L., Gaarde, M. B., Introduction to theory of high-harmonic generation in solids: tutorial. *J. Phys. B* **39**, 535-555 (2022).
4. Golde, D., Meier, T., Koch, S. W. High harmonics generated in semiconductor nanostructures by the coupled dynamics of optical inter- and intraband excitations. *Phys. Rev. B* **77**, 075330 (2008).
5. Gouliemakis, E., Brabec, T. High-harmonic generation in condensed matter. *Nature Phot.* **16**, 411–421 (2022).

6. Luu, T.T., Garg, M., Kruchinin, S. Yu., Moulet, A., Hassan, M. Th., Goulielmakis, E. Extreme ultraviolet high-harmonic spectroscopy of solids. *Nature* **521**, 498-502 (2015).
7. Vampa, G., Hammond, T. J., Thiré, N., Schmidt, B. E., Légaré, F., McDonald, C. R., Brabec, T., Klug, D. D., Corkum, P. B. All-optical reconstruction of crystal band structure. *Phys. Rev. Lett*. **115**, 193603 (2015).
8. Lanin, A. A., Stepanov, E. A., Fedotov, A. B., Zheltikov, A. M. Mapping the electron band structure by intraband high-harmonic generation in solids. *Optica* **4**, 516-519 (2017).
9. Yoshikawa, N., Tamaya, T., Tanaka, K. High-harmonic generation in graphene enhanced by elliptically polarized light excitation. *Science* **356**, 736–738 (2017).
10. Kobayashi, Y., Heide, C., Kelardeh, H. K., Johnson, A., Liu, F., Heinz, T. F., Reis, D. A., Ghimire, S. Polarisation flipping of even-order harmonics in monolayer transition-metal dichalcogenides. *Ultrafast Sci.* **2021**, 1–9 (2021).
11. Liu, H., Li, Y., You, Y. S., Ghimire, S., Heinz, T. F., Reis, D. A. High harmonic generation from an atomically thin semiconductor. *Nature. Phys.* **13**, 262–265 (2017).
12. Silva, R. E., Jiménez-Galán, A., Amorim, B., Smirnova, O., Ivanov, M. Topological strong-field physics on sub-laser-cycle timescale. *Nature. Phot.* **13**, 849–854 (2019).
13. Chacón, A., Kim, D., Zhu, W., Kelly, S. P., Dauphin, A., Pisanty, E., Maxwell, A. S., Picón, A., Ciappina, M. F., Kim, D. E., Ticknor, C., Saxena, A., Lewenstein, M. Circular dichroism in higher-order harmonic generation: heralding topological phases and transitions in Chern insulators. *Phys. Rev. B* **102**, 134115 (2020).
14. Bai, Y., Fei, F., Wang, S., Li, N., Li, X., Song, F., Li, R., Xu, Z., Liu, P. High harmonic generation from topological surface states. *Nature Phys*. **17**, 311–315 (2020).
15. Baykusheva, D., Chacón, A., Kim, D., Kim, D. E., Reis, D. A., Ghimire, S. Strong-field physics in three-dimensional topological insulators. *Phys. Rev. A* **103**, 023101 (2021).
16. Schmid, C. P., Weigl, L., Grössing, P., Junk, V., Gorini, C., Schlauderer, S., Ito, S., Meierhofer, M., Hofmann, N., Afanasiev, D., Crewse, J., Kokh, K. A., Tereshchenko, O. E., Güdde, J., Evers, F., Wilhelm, J., Richter, K., Höfer, U., Huber, R. Tunable non-integer high-harmonic generation in a topological insulator. *Nature* **593**, 385–390 (2021).
17. Herrmann, P., Klimmer, S., Lettau, T., Monfared, M., Staude, I., Paradisanos, I., Peschel, U., Soavi, G. Nonlinear All-Optical Coherent Generation and Read-Out of Valleys in Atomically Thin Semiconductors. *Small* **19**, 2301126 (2023).
18. Herrmann, P., Klimmer, S., Lettau, Weickhardt, T., Papavasileiou, A., Mosina, K., Sofer, Z., Paradisanos, I., Kartashov, D., Wilhelm, J., Soavi, G. Nonlinear valley

selection rules and all-optical probe of broken time-reversal symmetry in monolayer WSe_2. *Nature Phot.* **19**, 300-306 (2025).
19. Floss, I., Lemell, C., Wachter, G., Smejkal, V., Sato, S. A., Tong, X.-M., Yabana, K., Burgdörfer, J. *Ab initio* multiscale simulation of high-order harmonic generation in solids. *Phys. Rev. A* **97**, 011401(R) (2018).
20. Brown, G. G., Jiménez-Galán, A., Silva, R. E. F., Ivanov, M. A real-space perspective on dephasing in solid state high harmonic generation. Phys. Rev. Research **6**, 043005 (2024).
21. Brown, G. G., Jiménez-Galán, A., Silva, R. E. F., Ivanov, M. Ultrafast dephasing in solid state high harmonic generation: microscopic origin revealed by real-space dynamics. https://arxiv.org/abs/2310.17005.
22. Gonoskov, I., Tsatrafyllis, N., Kominis, I.K., Tzallas, P. Quantum optical signatures in strong-field laser physics: Infrared photon counting in high-order-harmonic generation. *Nature Comm*. https://doi.org/10.1038/srep32821 (2016).
23. Tsatrafyllis, N., Kominis, I.K., Gonoskov, I., Tzallas, P. High-order harmonics measured by the photon statistics of the infrared driving-field exiting the atomic medium. *Nature Comm*. https://doi.org/10.1038/ncomms15170 (2017).
24. Gorlach, A., Neufeld, O., Rivera, N., Cohen, O., Kaminer, I. The quantum-optical nature of high harmonic generation. *Nature Comm.* **11**, 4598 (2020).
25. Pizzi, A., Gorlach, A., Rivera, N., Nunnenkamp, A., Kaminer, I. Light emission from strongly driven many-body systems. *Nature Phys.* **19**, 551-561 (2023).
26. Tzallas, P. Squeezed light effect, *Nature Phot.* **17**, 463-464 (2023).
27. Ko, D.H., Corkum, P.B. Quantum optics meets attosecond science. *Nature Phys.* **19**, 1556-1557 (2023).
28. Rivera-Dean, J., Stammer, P., Maxwell, A.S., Lamprou, T., Ordóñez, A.F., Pisanty, E., Tzallas, P., Lewenstein, M., Ciappina, M. F. Nonclassical states of light after high-harmonic generation in semiconductors: A Bloch-based perspective. *Phys Rev B*, **109**, 035203 (2024).
29. Rasputnyi, A., Chen, Z., Birk, M., Cohen, O., Kaminer, I., Krüger, M., Seletskiy, D., Chekhova, M., Tani, F. High-harmonic generation by a bright squeezed vacuum. *Nature Phys.* **20**, 1960-1965 (2024).
30. Lemieux, S., Jalil, S.A., Purschke, D.N., Boroumand, N., Hammond, T.J., Villeneuve, D., Naumov, A., Brabec, T., Vampa, G. Photon bunching in high-harmonic emission controlled by quantum light. *Nature Phot.* **19**, 767-771 (2025).
31. Theidel, D., Cotte, V., Sondenheimer, R., Shiriaeva, V., Froidevaux, M., Severin, V., Merdji-Larue, A., Mosel, P., Fröhlich, S., Weber, K.-A., Morgner, U., Kovacev, M., Biegert, J., Merdji, H. Evidence of the Quantum Optical Nature of High-Harmonic Generation. *Phys. Rev. X Quantum* **5**, 040319 (2024).

32. Shiner, A. D., Trallero-Herrero, C., Kajumba, N., Bandulet, H.-C., Comtois, D., Légaré, F., Giguère, M., Kieffer, J-C., Corkum, P. B., Villeneuve, D. M. Wavelength scaling of high harmonic generation efficiency. *Phys. Rev. Lett*. **103**, 073902 (2009).
33. Liu, X., Li, L., Zhu, X., Huang, T., Zhang, X., Wang, D., Lan, P., Lu, P. Wavelength dependence of high-order harmonic yields in solids. *Phys. Rev. A* **98**, 063419 (2018).
34. Ninomiya, S., Adachi, S., Optical properties of cubic and hexagonal CdSe. *J. Appl. Phys*. **78**, 4681-4689 (1995).
35. Barati, F., Grossnickle, M., Su, S., Lake, R. K., Aji, V., Gabor, N. M. Hot carrier-enhanced interlayer electron–hole pair multiplication in 2D semiconductor heterostructure photocells. *Nature Nanotech.* **12**, 1134-1139 (2017).
36. Kim, Ji-H., Bergren, M. R., Park, J. C., Adhikari, S., Lorke, M., Frauenheim, T., Choe, D.-H., Kim, B., Choi, H., Gregorkiewicz, T., Lee, Y. H. Carrier multiplication in van der Waals layered transition metal dichalcogenides. *Nature Commun.* https://doi.org/10.1038/s41467-019-13325-9 (2019).
37. Zheng, W., Bonn, M., Wang, H. I. Photoconductivity multiplication in semiconducting few-layer $MoTe_2$. *Nano Lett.* **20**, 5807-5813 (2020).
38. He, G., Nathawat, J., Kwan, C.-P., Ramamoorthy, H., Somphonsane, R., Zhao, M., Ghosh, K., Singisetti, U., Perea-López, N., Zhou, C., Elías, A. L., Terrones, M., Gong, Y., Zhang, X., Vajtai, R., Ajayan, P. M., Ferry, D. K., Bird, J. P. Negative differential conductance & hot-carrier avalanching in monolayer WS_2 FETs. *Nature Scientific Rep.* DOI:10.1038/s41598-017-11647-6 (2017).
39. D. K. Ferry. Electron transport in some transition metal dichalcogenides: MoS_2 and WS_2. *Semicond. Sci. Technol.* **32**, 085003 (2017).
40. Heide, C., Kobayashi, Y., Johnson, A. C., Liu, F., Heinz, T. F., Reis, D. A., Ghimire, S. Probing electron-hole coherence in strongly driven 2D materials using high-harmonic generation. *Optica* **9**, 512-516 (2022).
41. Keldysh, L. V. Ionization in the field of a strong electromagnetic wave. *Sov. Phys. JETP* **20**, 1307-1314 (1965).
42. Laser induced damedge in optical materials. Edited by D. Ristau, CRC Press, ISBN 13: 978-1-138-19956-9, 2016.
43. Schiessl, K., Ishikawa, K. L., Persson, E., Burgdörfer, J. Quantum Path Interference in the Wavelength Dependence of High-Harmonic Generation. *Phys. Rev. Lett.* **99**, 253903 (2007).
44. Giannozzi, P., Baseggio, O., Bonfà, P., Brunato, D., Car, R., Carnimeo, I., Cavazzoni, C., de Gironcoli, S., Delugas, P., Ruffino, F. F., Ferretti, A., Marzari, N., Timrov, I., Urru, A., Baroni, S. QUANTUM ESPRESSO toward the exascale. *Jorn. Chem. Phys.* **152**, 154105 (2020); http://www.quantum-espresso.org
45. Hamann, D. R. Optimized norm-conserving Vanderbilt pseudopotentials**.** *Phys. Rev. B* **88**, 085117 (2013).

46. Schlipf, M., Gygi, F. Optimization algorithm for the generation of ONCV pseudopotentials. *Comp. Phys. Commun.* **196**, 36-44 (2015).
47. Perdew, J. P., Burke, K., Ernzerhof, M. Generalized Gradient Approximation Made Simple. *Phys. Rev. Lett.* **77**, 3865-3868 (1996).
48. Giustino, F., Cohen, M. L., Louie, S. G. Electron-phonon interaction using Wannier functions. *Phys. Rev. B* **76**, 165108 (2007).
49. Poncé, S., Margine, E. R., Verdi, C., Giustino, F. EPW: Electron–phonon coupling, transport and superconducting properties using maximally localized Wannier functions. *Comput. Phys. Commun*. **209**, 116-133 (2016).
50. Mahatha, S. K., Ngankeu, A. S., Frank Hinsche, N., Mertig, I., Guilloy, K., Matzen, P. L., Bianchi, M., Sanders, C. E., Miwa, J. A., Bana, H., Travaglia, E., Lacovig, P., Bignardi, L., Lizzit, D., Larciprete, R., Baraldi, A., Lizzit, S., Hofmann, P. Electron–phonon coupling in single-layer MoS_2. *Surf. Sci.* **681**, 64-69 (2019).
51. Tancogne-Dejean, N., Oliveira, M. J. T., Andrade, X., Appel, H., Borca, C. H., Le Breton, G., Buchholz, F., Castro, A., Corni, S., Correa, A. A., De Giovannini, U., Delgado, A., Eich, F. G., Flick, J., Gil, G., Gomez, A., Helbig, N., Hübener, H., Jestädt, R., Jornet-Somoza, J., Larsen, A. H., Lebedeva, I. V., Lüders, M., Marques, M. A., L., Ohlmann, S. T., Pipolo, S., Rampp, M., Rozzi, C. A., Strubbe, D. A., Sato, S. A., Schäfer, C., Theophilou, I., Welden, A., Rubio, A. Octopus, a computational framework for exploring light-driven phenomena and quantum dynamics in extended and finite systems. *Journ. Chem. Phys.* **152** 124119 (2020).
52. Hartwigsen, C., Goedecker, S., Hutter, J. Relativistic separable dual-space Gaussian pseudopotentials from H to Rn. *Phys. Rev. B* **58**, 3641-3662 (1998).
53. Liu, G.-B., Shan, W.-Y., Yao, Y., Yao, W., Xiao, D. Three-band tight-binding model for monolayers of group-VIB transition metal dichalcogenides. *Phys. Rev. B* **88**, 085433 (2013).

Supplementary Files

This is a list of supplementary files associated with this preprint. Click to download.

- KorolevSupplementaryNaturePhot.pdf